Sustainable Materials and Technologies 37 (2023) e00692

Contents lists available at ScienceDirect

Sustainable Materials and Technologies

journal homepage: www.elsevier.com/locate/susmat

Large-scale fabrication of superhydrophobic shape memory composite films for efficient anti-icing and de-icing

Xinlin Li [a], Yanju Liu [b,*], Jinsong Leng [a,*]

[a] Centre for Composite Materials and Structures, Harbin Institute of Technology (HIT), Harbin 150080, PR China
[b] Department of Astronautical Science and Mechanics, Harbin Institute of Technology (HIT), Harbin 150001, PR China

ARTICLE INFO

Keywords:
Shape memory polymer
Photothermal effect
Superhydrophobicity
Anti-icing
de-icing

ABSTRACT

Ice and snow accretion on outdoor facilities may degrade their functions and reduce their service life. Superwetting materials have been widely studied and present high potential in anti-icing and de-icing applications. However, it remains challenging that the materials cannot prevent and remove the ice accretion spontaneously in harsh conditions. Penguins can freely jump in and out of extremely cold water (−40 °C) without forming macroscopic ice because of the superhydrophobic performance of their flexible feathers. Here, Penguins-inspired superhydrophobic shape memory composite films with unique properties, including lightweight and shape morphing, are fabricated via a two-step method consisting of spraying and peeling processes. It presents good superhydrophobic performance with a large WCA of 152.4 ± 5° and a small WSA of 6 ± 1° in addition to excellent shape memory performance (recovery ratio > 99%) and good mechanical strength. The simple fabrication methods make it possible to produce large-size films at low cost, which is versatile for different applications. Most importantly, the film displays the capabilities of inhibiting freezing, ice, and snow accumulation with improved ice removal efficiency due to the synergetic effects of the superhydrophobic and efficient photothermal activity. Furthermore, its robustness and durability make it a good candidate for industrial applications.

1. Introduction

Ice and snow accumulation often cause serious impacts on transportation [1], powerlines [2], solar panels [3], aircrafts [4], etc. The commonly used methods, including physical [5,6], and chemical methods [7], are not effective enough in removing the ice bulk and consume a large amount of energy. Hence, developing effective and reliable anti-icing or de-icing techniques is becoming a hot topic [8–10]. Inspired by nature's unique wetting and dewetting phenomena, some functional materials have been proposed as the best candidates for anti−/de-icing applications. For example, lotus leaves-like superhydrophobic materials presented good anti-icing performance [11] due to the effective propelling of cold-water droplets before freezing [12], prolonging the icing time [13], and reducing the ice adhesion strength [14]. However, such materials may suffer from the drawbacks of being fragile and brittle at ultralow temperatures, which limit their application potentials, although recent studies have improved the physical and chemical robustness [15–18] and the stabilities of the icephobicity under extreme conditions [19,20]. Hence, achieving completely ice-free property with good long-term performance is important to satisfy the demand in real applications.

Materials with anti-icing and de-icing properties are becoming more and more popular in the future [21–23]. It requires preventing the adhesion of supercold water droplets and accelerating their repellency before being frozen during the anti-icing process. In addition, the materials can actively melt or remove the accumulated ice. Therefore, specially designed functional materials have been proposed with unique properties, such as electrothermal [24,25], magnetothermal [26,27], and photothermal [28,29] activities. For example, Li et al. [24] reported a transparent electrothermal material using wrinkled graphene, achieving quick defogging, low energy consumption, and good robustness. To avoid using electricity, Wu et al. [29] proposed a transparent, photothermally icephobic surface coating, which could effectively convert ubiquitous sunlight to heat to remove frost or ice. Dash et al. [30] created a multilayered de-icing photothermal trap laminate consisting of a selective solar absorber, a thermal spreader, and an insulation layer to reduce heat loss. The laboratory and outdoor experiments demonstrated the removal performance of different types of ice, like

---

* Corresponding authors.
E-mail addresses: yj_liu@hit.edu.cn (Y. Liu), lengjs@hit.edu.cn (J. Leng).

https://doi.org/10.1016/j.susmat.2023.e00692
Received 13 January 2023; Received in revised form 9 June 2023; Accepted 11 August 2023

frost, frozen droplets, and snow, over a large surface area under gravity or aerodynamic forces. Although significant progress in functional de-icing materials has been made, it should be noticed that these materials, as two-dimensional (2D) anti−/de-icing materials, cannot actively remove the ice by changing their shapes if the freezing water is static.

Penguins are representative animals living in the Antarctic, where the wind speeds are 40 m/s, and the air temperatures and water temperatures are about −40 °C and − 2.2 °C, respectively. They frequently dive in and out of cold water during the frigid winter without forming macroscopic ice on their feathers [31] due to their unique surface chemistry and physical structures. The glands of their feather could release grease as the superhydrophobic layer for repelling water droplets while reducing ice adhesion, resulting in excellent de-icing performance [32]. Noticeably, the penguins frequently change the shape of their feathers when they are in and out of water. This mechanical deformation of the surface is also essential for dewetting and de-icing. Inspired by this, a novel 3D anti−/de-icing material is designed by combining photothermal performance and mechanical shape change behavior with a superhydrophobic material, which could be developed for future anti−/de-icing applications.

Shape memory polymer (SMP) and composites are representative smart materials capable of changing their shape under external stimuli [33,34], including electricity [35], magnetic field [36], light [37], and water [38]. It is known that morphology and chemicals are two main factors that dominate surface wettability [39]. The design of the 3D anti−/de-icing material is based on developing a superhydrophobic SMP material with photothermal effects. The SMP composites are widely studied in tuning the surface wettability due to the ability to memorize any shapes of the structures at multiple dimensions [40,41]. Wang et al. [42] reported a shape memory superhydrophobic micropillar surface structure with a switchable wettability controlled by applying the external force and voltage bias. The active de-icing material exhibited good electrothermal properties with excellent thermal conductivity. Chen et al. [43] prepared the shape memory GO/EP composites with high anti−/de-icing efficiency. It illustrated that the solid ice could be removed due to the active deformation of shape memory GO/EP composites, resulting in the self-removal of ice. Nevertheless, the anti-icing and de-icing performance of shape-morphing superwetting materials is less reported, although it can be expected that the combination of superwettability and SMP composites present two advantages in achieving de-icing. First, it can effectively prevent water adhesion and ice accretion. Meanwhile, shape-changing can be conducive to de-icing by reducing the ice adhesion while actively removing ice deposition. Furthermore, shape memory materials can be widely applied in diverse industrial areas utilizing low-cost and large-scale spraying methods. [44,45]

In this work, we developed the MWCNT-reinforced superhydrophobic shape memory composite films with photothermal activity. The composite films present good superhydrophobic properties (WCA ~ 152.4 ± 5° and WSA ~ 6 ± 1°) with excellent shape memory performance (recovery ratio > 99%), which can be actuated by different stimuli, like heat, IR light, and hot water. The thin film is lightweight but with good mechanical strength. Its excellent light absorption across a wide wavelength range made it a good candidate for photothermal effects. The composite films exhibited excellent outdoor anti-icing and de-icing properties while maintaining good durability after repeating harsh fatigue tests, including thermal cycles, boiling, abrasion, water flush, and pressed by heavy loading. The simple and low-cost large-scale fabrication of the superhydrophobic shape memory composite films via spraying methods makes them commercially viable in industrial anti-icing and de-icing applications.

2. Experimental section

2.1. Materials and methods

Multi-walled carbon nanotubes (MWNTs) were purchased from Suzhou Tanfeng Graphene Technology Corporation. 1H,1H,2H,2H-perfluorooctyltrimethoxysilane (PFOTS) and ethyl acetate (EA), PDMS (Sylgard 184), and its curing agent were obtained from Shanghai Macklin Biochemical Corporation. The shape memory epoxy resin (SMEP) was made from bisphenol A-type epoxy resin and Jefamine D230 in our lab, which were purchased from Shanghai Macklin Biochemical Corporation.

2.2. Fabrication of the superhydrophobic film

The preparation process of the superhydrophobic film is illustrated in Fig. 1. Firstly, a certain amount of MWNTs (0.5, 0.55, 0.6, 0.65, 0.7, and 0.75 g, respectively) was dispersed in 100 mL EA, followed by magnetic stirring for 5 min. The samples were labeled as MWNT-0.5, MWNT-0.55, MWNT-0.6, MWNT-0.65, MWNT-0.7, and MWNT-0.75, respectively. PFOTS was added into the suspension dropwise to a total of 1 wt%. After stirring for 12 h, 6 g SMEP was fully dissolved in the solution by magnetic stirring for another 12 h. Then, 2 g PDMS was added to the solution and magnetically stirred for 12 h. Before spraying, PDMS curing agents (0.2 g) were added and stirred for 2 h. The as-prepared solution was sprayed with compressed air (2–4 MPa) onto the glass plate covered by release cloth. The spraying distance was about 15 cm, and the spraying gun was moved at a speed of 5 cm/s. Afterward, the coating was cured at 100 °C for 2 h. Finally, the superhydrophobic film was detached from the glass plate. As the control group, the superhydrophobic films without either SMEP or PDMS were fabricated with the same method, in which 0.7 g of the PFOTS-modified MWNTs were added.

2.3. Sample characterization

2.3.1. Morphology, chemicals, and wetting states characterization

The surface morphologies and chemicals of the films were investigated by scanning electron microscopy (SEM, TESCAN AMBER, Czech), X-ray photoelectron spectroscopy (XPS, Kratos, UK), Energy Dispersive Spectroscopy (EDS, Oxford Ultimately MAX40, UK), and Fourier Transform Infrared Spectroscopy (FTIR, PerkinElmer L1600400, USA), respectively. The surface roughness was measured by 3D optical microscopes (Bruker Contour GT-X, Germany). The surface wetting behavior was evaluated by water contact angles (θ_{CA}, WCA) and sliding angles (θ_{SA}, WSA). The values were measured by a contact angle meter (Shengding-100S, China) at an ambient temperature of 23 ± 2 °C, and the tested volume of water droplets was 5 μL.

2.3.2. Shape-memory behavior characterization

Differential scanning calorimetric (DSC, NETZSCH STA 449 F3, Germany) data were recorded from 25 to 200 °C under a nitrogen atmosphere, where the heating rate was 10 °C/min. Dynamic thermomechanical analysis (DMA) was employed to investigate the thermomechanical properties of the samples between 25 and 200 °C at a heating rate of 3 °C/min under strain applied at the constant frequency of 1 Hz.

To evaluate the shape recovery performance, the film was cut into a rectangular shape (10 × 30 mm^2). It was bent into a "U" shape above the T_g and quickly fixed in the temporary shape after cooling to room temperature under external force. The shape recovery was actuated and recorded when the deformed films were heated to 100 °C. During the recovery, the change of the deformation angle, θ(t), was recorded from the photographs using Digimizer software. The recovery ratio (R) is defined as follows [46]:

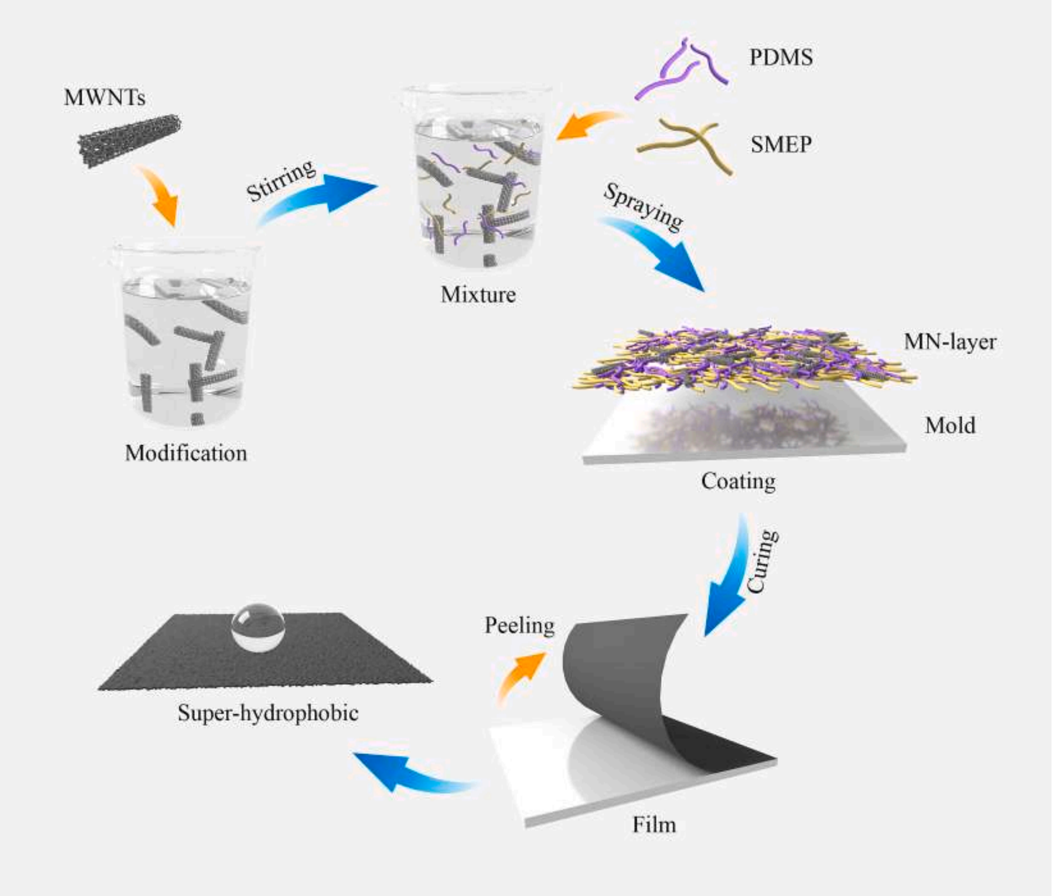

Fig. 1. Schematic of the preparation process of the superhydrophobic film through the spraying method.

$$R\% = \frac{\theta(t) - \theta_0}{180 - \theta_0} \tag{1}$$

where θ_0 is the deformation angle at the time of 0 s.

2.3.3. *Light absorption characterization*

The diffuse reflectance UV–Vis-NIR spectrophotometer (UV-3600-plus, Shimadzu) was utilized to evaluate the light absorption performance in the wavelength range of 200–2500 nm. The visible light absorption was measured by UV–Vis spectrophotometer (UV-2600, Shimadzu) and the wavelength range was 200–1400 nm.

2.3.4. *Anti-icing and de-icing test*

All outdoor tests were carried out in winter in Harbin, China. The freezing times of both bare aluminum plate and that covered with the SMEP composite films were recorded by placing 50 μL water droplets on the surfaces at the environment temperature of −15 °C. The de-icing tests were carried out by observing the ice melting process from the samples illuminated by infrared light (808 nm, 1 W). And the icing/de-icing cycles of as-prepared composite film was investigated by immersing in water and iced in refrigerator for 12 h, followed by the evolution of wettability. The anti-icing and de-icing tests of freezing rain, snow, and hybrid situations were also evaluated on the wings of a model aluminum airplane, with the temperature recorded by a hand-held thermal camera (HIKMICRO H21, China).

2.3.5. *Robustness and durability test*

The durability of the superhydrophobic property under thermal shock was tested by immersing the composite films in boiling water for 5 min, followed by measuring the θ_{CA} and θ_{SA}. The chemical stability was investigated by measuring the θ_{CA} and θ_{SA} at different pH. The abrasion test was also investigated by directly pulling and scuffing the film on sandpaper (grit #360) along a fixed direction. Each abrasion cycle was carried out with a displacement of 10 cm at a speed of 2 cm/s under the loading of 100 g. After several abrasion cycles, the changes in surface wettability were evaluated by the θ_{CA} and θ_{SA} values. A water flushing test was carried out by placing the superhydrophobic film under the tap with an impacting pressure of ~2.5 kPa. The resultant θ_{CA} and θ_{SA} were measured every 5 min.

3. Results and discussion

3.1. *Surface morphology, chemicals, and wettability*

The spray method is widely used in the fabrication of coatings and films. As shown in Fig. 1, the superhydrophobic coating was directly sprayed on the glass plate and peeled off after being cured. This simple fabrication method doesn't require sophisticated equipment while easily obtaining large area samples to satisfy the wide demand. The multi-scale structures are essential in achieving the superhydrophobic surface. Fig. S1 shows that the surface morphology became rougher with the increase in MWNTs.Meanwhile, the WCA was increased while the WSA was decreased, as shown in Fig. 2d. The best superhydrophobicity was obtained from the MWNT-0.75 with maximum θ_{CA} of153.9 ± 6° and minimum θ_{SA} of 6 ± 1°. However, the MWNT-0.75 film is too fragile to be peeled off in one piece. Instead, the MWNT-0.7 film was selected for further tests with the θ_{CA} of 152.4 ± 5° and θ_{SA} of 6 ± 1° since it exhibited good tensile strength. Fig. 2a shows the irregular micro protrusions on the superhydrophobic MWNT-0.7 film due to the stacking of MWNTs. The magnified SEM images in Figs. 2b and c revealed that some

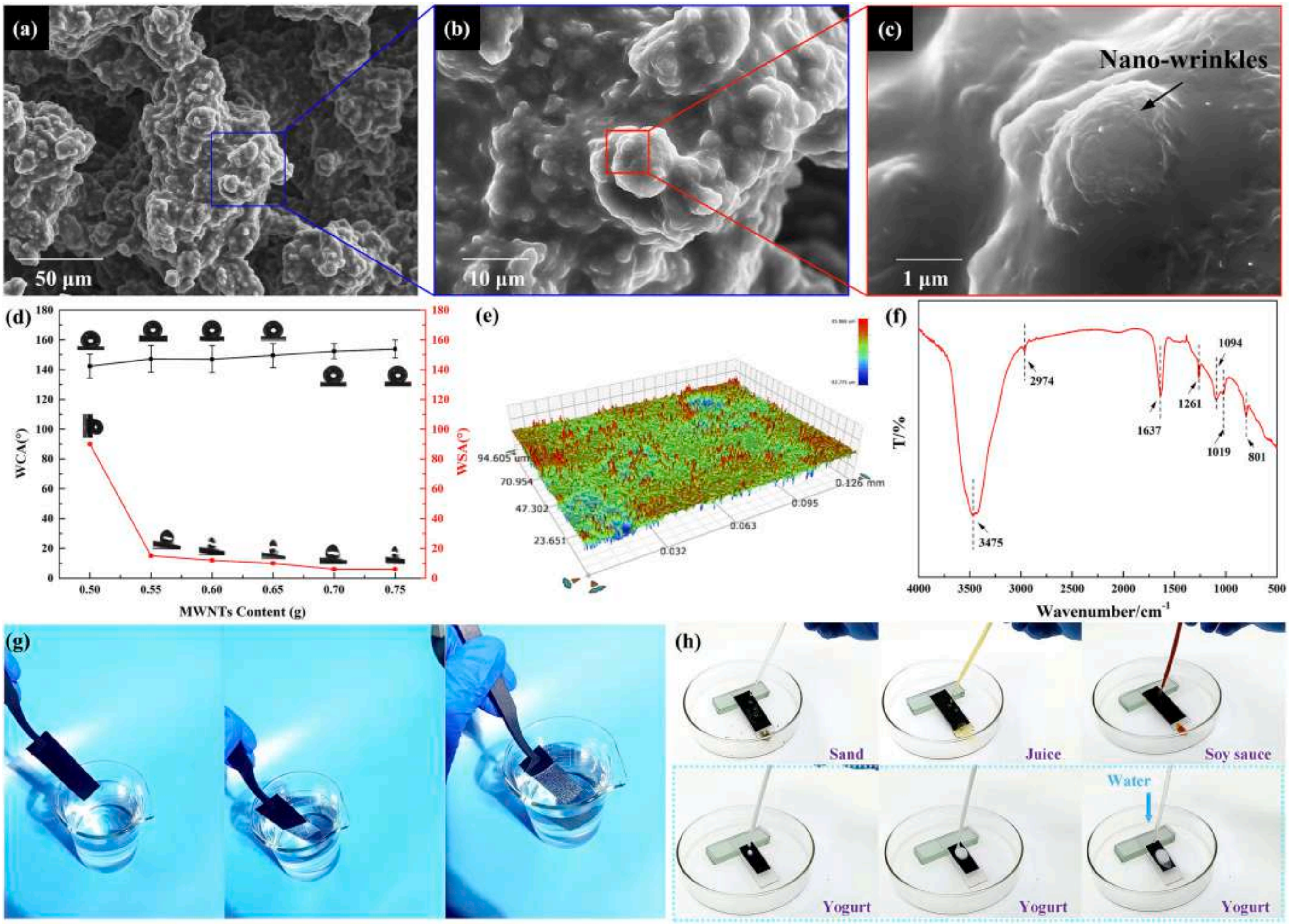

Fig. 2. The investigation of superhydrophobic film of MWNT-0.7. (a) - (c) SEM images at different magnifications 500×, 2kx, and 20kx, respectively. (d) Wettability test: water contact angle (WCA) and water sliding angle (WSA) as a function of MWCNT contents. (e) Surface roughness image from a 3D optical microscope. (f) FT-IR spectrum of MWNT-0.7. (g) Immersion of the film in water. (h) Self-cleaning test: juice (high sugar content), soy sauce (high salt content), and yogurt (high protein content).

nano-wrinkles covered the micro-hemispheres on the protrusions. The surface roughness (Ra) of the MWNT-0.7 film was about 7.075 μm from the 3D optical microscopic image in Fig. 2e.

The chemical composition is another factor that determines the superhydrophobic property. The FT-IR spectra of MWNT-0.7 composite film in Fig. 2f show two absorption peaks at 1094 and 801 cm^{-1} associated with the bending and stretching vibrations of Si-O-Si bonds. The peak at 1637 cm^{-1} could be assigned to the skeleton vibrations of the benzene ring in the EP main chain [47]. The peaks at 3475 and 2974 cm^{-1} are assigned to O—H and C—H stretching vibrations, respectively. The presence of -OH could be attributed to the absorbed H_2O. The peak at 1261 cm^{-1} is attributed to the -CF_3 symmetric stretching vibration, indicating that the fluorine groups successfully modified the MWNTs [48]. The existence of fluorine elements on the outer layer of the embedded MWNTs was also confirmed by XPS, as shown in Fig. S2. The strong signals of silicon (Si), carbon (C), oxygen (O), and fluorine (F) were observed at 102, 284, 532, and 688 eV, respectively. Table S1 presents the atomic ratios of the four elements in the composite film, where the high atomic ratio of fluorine is essential in achieving superhydrophobicity.

The superhydrophobic property of the MWNT-0.7 composite film is also demonstrated by the air trapped on the surface of the film when it is immersed in water. Fig. 2g shows the bright mirror formed at the surface due to the reflection of light by the air layer, indicating the air cushion was formed at the interface. Fig. 2h and supporting video 1 also demonstrated the low adhesion of particles on the surface. At the tilt angle of 7°, the deposited sand grits were easily removed by several water droplets. In addition, the liquid droplets with different viscosities are entirely rolled off the film without contamination, such as juice (high sugar content), soy sauce (high salt content), and yogurt (high protein content). Due to the high viscosity of yogurt, it takes longer to slide off, but the process can be accelerated by applying water droplets. The results confirmed the superhydrophobic property of the composite film with good self-cleaning behavior. Hence it was selected for further investigation.

3.2. Shape memory properties

More interestingly, the shape memory of the superhydrophobic film can be actuated by external stimuli, such as heat and infrared light. The dynamic thermomechanical test evaluated the thermodynamic properties of the SMEP and MWNT-0.7 composite film. Fig. 3a shows the temperature-dependent storage modulus (E`) analyzed by DMA. With the increase in temperature, both samples showed a change of stiffness with the E` values degraded significantly, which contributed to the excellent shape memory behaviors [49]. In addition, the E` of the MWNT-0.7 composite film (380 Mpa) is 4 times lower than that of the SMEP (>1600Mpa), which could be attributed to the interfacial interaction that existed between the nanotubes and the SMEP matrix [50], or the restriction of relative displacement of molecular segment [51]. The

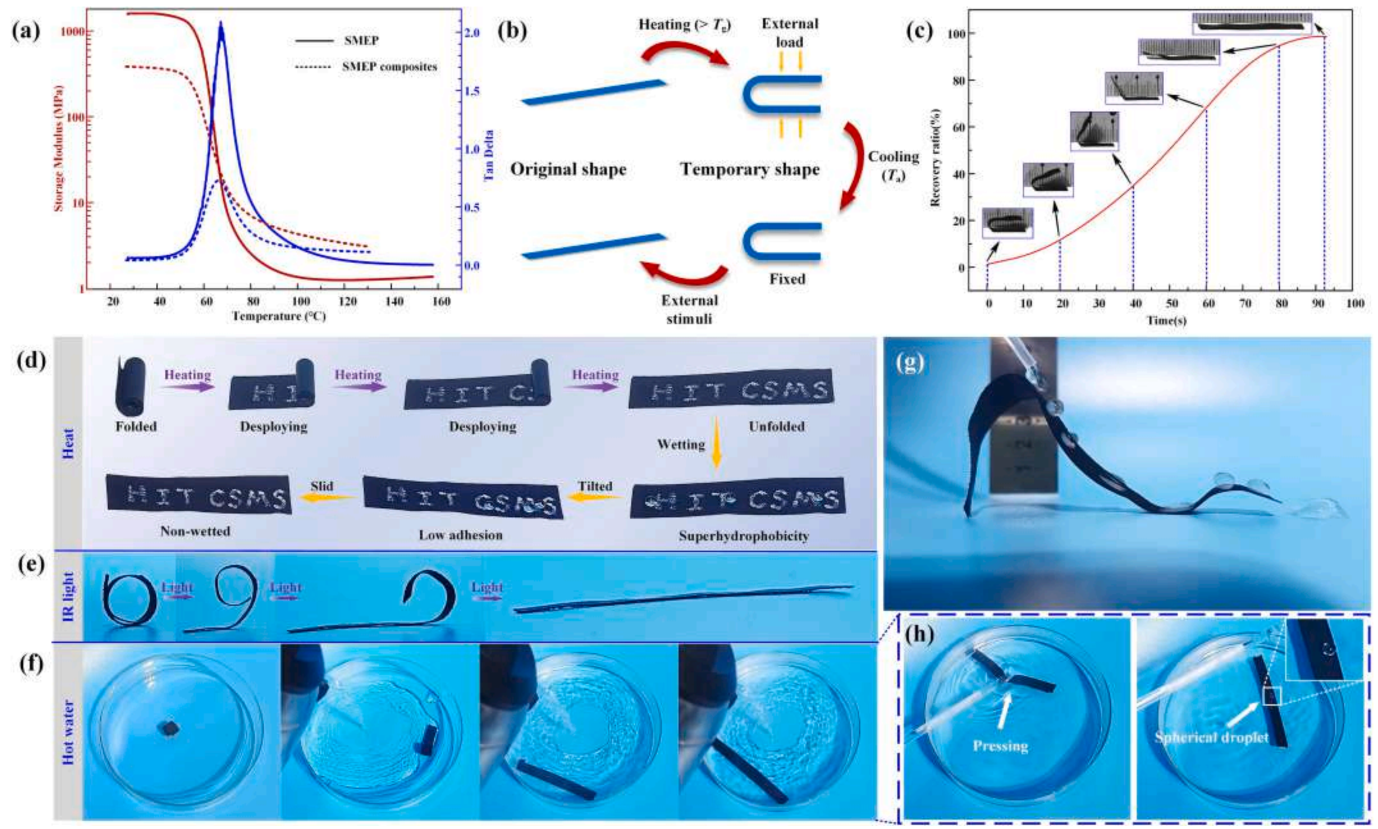

Fig. 3. (a) DMA curves of SMEP and MWNT-0.7 films; (b) Schematics of the shape recovery process; (c) Shape recovery ratio curve of the MWNT-0.7 film, insets are the real-time changes of the shape recovery process; (d) - (f) Shape memory test with external stimuli of heat, IR light, and hot water, respectively; (g) Variable stiffness and superhydrophobicity test of SMEP composite films; (h) Lotus leaf effect of the SMEP composite films in hot water pool.

decrease in the E` value could also be related to the dilution of SMEP due to the addition of MWNTs. The peak of loss factor (Tan δ) suggests that the glass transition temperatures (T_g) of pure SMEP and MWNT-0.7 composite films are 67 and 66 °C, respectively. The results indicate that PDMS and CNT have less effect on the T_g. The schematic diagram in Fig. 3b shows the measurement of the shape memory effect. The samples were folded into a "U" shape under external loads with temperatures above T_g. When the temperature was decreased below the T_g, the folded shape is fixed (memorized) even after removing the load. Once external stimuli are applied to the sample, like heat, IR light, or magnetic, it can be triggered to recover to its original shape.

The heat-triggered shape-memory test is employed to characterize the shape recovery ratio, and the insets in Fig. 3c display the real-time shape changes of the SMEP composite film (MWNT-0.7). The original shape was recovered within 89 s with a recovery ratio of over 99%, indicating its excellent shape memory effect. Employing this unique character, the SMEP composite film can be folded into a temporary scroll shape with no need for fastening rings; see supporting video 2. As shown in Fig. 3d, the film was written with characters of "HIT CSMS" (Harbin Institute of Technology, Center for Smart Materials and Structures) before being folded. When heated above the T_g, the scroll deployed gradually and recovered to its original shape. Even at a temperature above the T_g, the superhydrophobic property was maintained as the water droplets formed in a ball shape and easily slid off the surface. In addition, the surface property was not degraded by repeating water washing; hence it is suitable for long-term outdoor applications. The shape memory effect can also be triggered by illumination with near-infrared light ($\lambda = 808$ nm, 1 W). As shown in Fig. 3e, the ring of SMEP composite film can be contactless activated and selectively deployed by controlling the location of light illumination. The curved SMEP composite film recovered to its original shape after submerging in hot water (> 90 °C), as shown in Fig. 3f. Interestingly, the floating film could not be pressed into a hot water pool, and the water droplet was formed in a spherical shape, as shown in Fig. 3h. This unique property offers the possibility of designing a large deployable platform on the water. As ultra-thin, the MWNT-0.7 composite film can be morphed into any shape, for example, a triple-folded "M" shape (see Fig. 3g). Due to its excellent superhydrophobic properties, water droplets quickly slid down along the film. Additionally, the variable stiffness property endowed the film to undertake the impacting force of water droplets without external supporting structures. Therefore, enormous-sized films can be potentially designed as deployable habitation cabins.

3.3. *Lightweight, mechanical and photothermal properties*

The SMEP composite films also present a lightweight property. As shown in Fig. 4a, the composite film was easily suspended when placed on a dandelion. The measured density is as low as 0.78 g·cm^{-3}, presenting its ultra-low weight property. From the SEM image of its cross-section (see Fig. 4b), it is revealed that the film is composed of a basic layer and a hierarchical structure. The thickness of a basic layer is approximately 180 μm, acting as the holding layer. To investigate the mechanical property of the thin film, a series of experimental studies were carried out; see supporting video 3. As shown in Figure 4c$_{I}$, the SMEP composite films could withstand a total weight of 1.5 kg before the film (10 mm × 50 mm) was broken, similar to a single SMEP@CNT0.7 film (Figure 4c$_{III}$). However, it presented a better mechanical property than the single PDMS@CNT 0.7 film, which can only bear the total load of 300 g, see Figure 4c$_{II}$. After sharp pressing and stretching 25 times, the SMEP composite film kept its integrity and superhydrophobicity, as shown in Fig. 4d. It revealed that SMEP composite film presented good mechanical strength even with a small

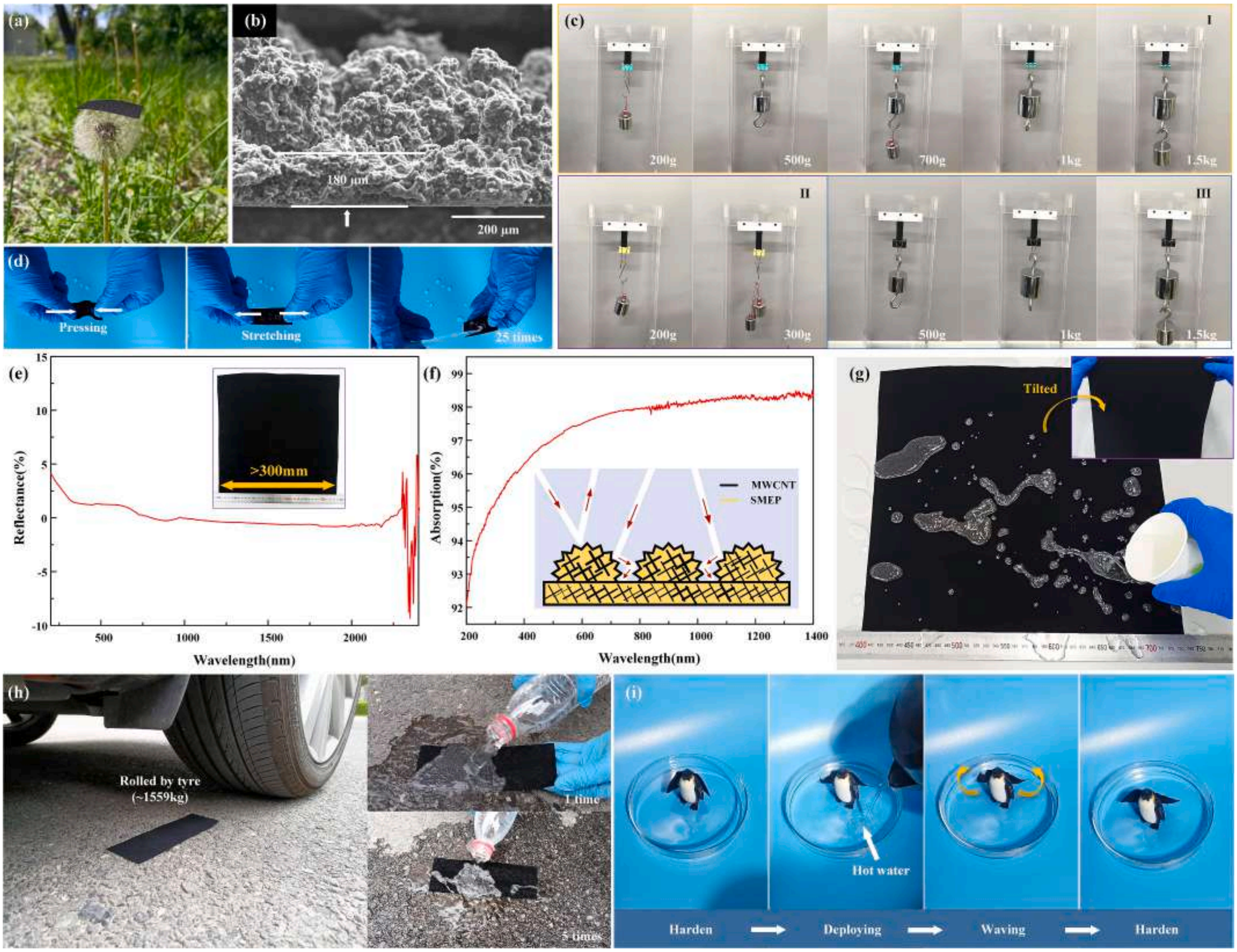

Fig. 4. (a) The composite film placed on dandelion; (b) SEM image of the cross-section of the film; (c) Tensile tests of SMEP composite film, PDMS@CNT 0.7 film, and SMEP@CNT0.7 film respectively; (d) Sharp pressing and stretching test of SMEP composite film; (e) Visible-near infrared (UV–vis-NIR) absorption spectra of SMEP composite film between 250 and 2500 nm; (f) Absorption spectrum between 400 and 1400 nm; (g) Superhydrophobicity of large-scale SMEP composite film; (h) Repeatedly rolled by a vehicle (weight of ≈1559 kg), (i) SMEP composite cape of penguin.

thickness.

Besides, the hierarchical structures of the MWCNT layer acted as the functional layer, contributing to the maximum light absorption. The reflectance of the SMEP composite film across the UV–vis-NIR region with a wavelength between 250 and 2500 nm is shown in Fig. 4e. The reflectance of the MWNT-0.7 film gradually decreased as the wavelength of light increased. Especially, the reflectance decreased below 0.1% at the wavelength of 785–2300 nm. Its unique light absorption ability at the NIR region is beneficial for de-icing applications with sunlight-driven photothermal conversion. The SMPE composite film can be fabricated large-scale for practical applications using the standard spray coating. As shown in the insets of Fig. 4e, the film was fabricated with a side length longer than 300 mm, restricted by the mold size.

Moreover, the visible light absorption property was also investigated, as shown in Fig. 4f. It showed that the overall absorptions of specific wavelengths between 400 and 1400 nm were higher than 95%, which is attributed to the hierarchical micro-nano structures. Especially, 98% of the light near 808 nm was absorbed, indicating good IR absorption performance, which is important for the photothermal performance. The strong light absorption was achieved via light trapping and decreased Fresnel reflection [52], as illustrated in the insets of Fig. 4f. In addition, the films displayed uniform and excellent functional properties even at a large scale. When a cup of water was poured onto a film of large size, as shown in Fig. 4g and supporting video 4, water droplets quickly slid off after hung up, presenting good superhydrophobic and water-repelling properties. The film was placed on the rough ground to testify to its mechanical robustness, and a vehicle (its total weight over 1559 kg) was slowly run over it. There was no obvious damage to the film even after rolling over 5 times, although it was covered with numerous bumps and pits (see Fig. 4h and Fig. S3). Meanwhile, the composite film cannot be wetted even washed by water, proving that the hierarchical structure was preserved.

Based on its variable stiffness, good superhydrophobicity, and mechanical properties, it could be designed as a new type of smart cape for body protection. Compared with conventional silk capes, the composite cape exhibited two specific features. At a defensive state (room temperature), the composite cape can tightly wrap the penguin as a shield, protecting the penguin from chemical and physical damage, as shown in Fig. 4i. In a casual state, the cape slowly deployed and recovered to its original shape when it was heated (hot water injected). The shapes could be fixed without needing external force after their temperature decreased below the T_g. Meanwhile, this property also enables the composite film to be easily adhered and glued onto facilities` surfaces with diverse shapes for protection. It can be foreseen that the SMEP composite film can be widely used in various potential applications because of its multifunctional properties.

3.4. Anti-icing and de-icing properties

The surfaces of outdoor facilities should have anti-icing and de-icing properties to keep them ice-free. Anti-icing is achieved by preventing the accumulation of water droplets before they are frozen by rolling off driven by wind, gravity, and vibration. Surfaces can achieve good de-icing properties if they can remove the ice smartly and actively. To evaluate the anti-icing and de-icing performance, the SMEP composite films were adhered onto an aluminum plate by thin double-layered sticking tapes and placed outdoors at the environmental temperature of −15 °C. For comparison, the bare aluminum plate was simultaneously placed in the same conditions. Afterward, 50 μL water droplets were dropped on both sample surfaces, and the freezing process was recorded in Fig. 5a. It was found that the deposited water droplet quickly spread on the bare aluminum plate and was frozen into ice within 31 s. But the icing process was greatly delayed on the MWNT-0.7 composite film, where water droplets completely froze after 292 s, about 10 times longer than that on the bare aluminum plate. During the frozen process, water droplets preserved the spherical shape, significantly reducing the ice-solid contact area and resulting in slow thermal energy transfer and ice formation. Therefore, the formed ice could also be easily removed

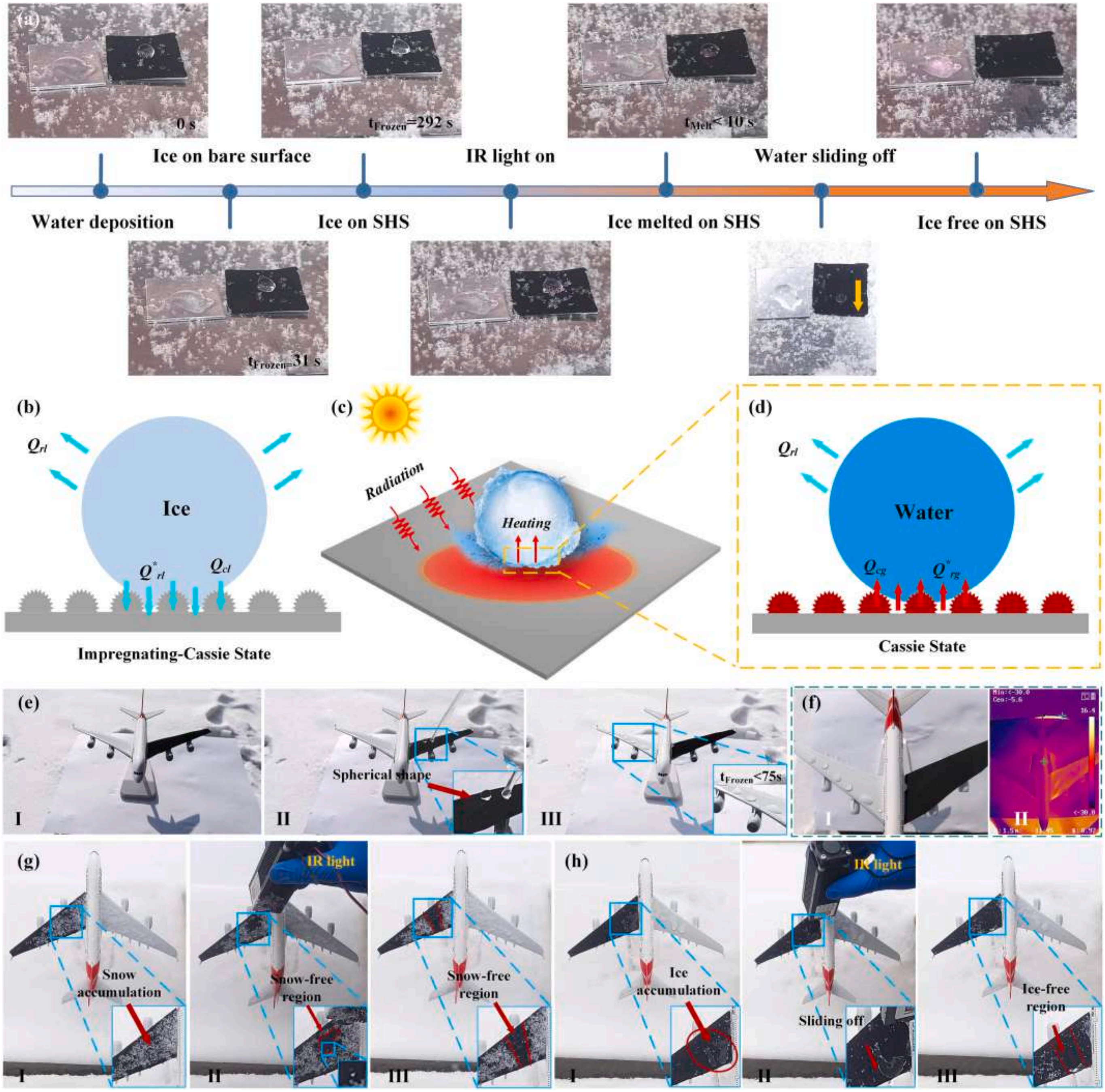

Fig. 5. (a) Anti-icing and de-icing test on bare aluminum plate and that covered by SMEP composite films at −15 °C; (b)-(d) heat transfer model of anti-icing and de-icing process respectively; (e) Freezing rain test of the wings of an airplane model with or without SMEP composite films at −14 °C and (f) the thermography of airplane model; (g) Snow test and (h) hybrid test of the freezing rain of airplane model with or without SMEP composite films at −10 °C.

from the surface by surface movements, including wind, gravity, and vibration. Furthermore, the de-icing property is another advantage of composite films. When the infrared light was applied to the composite film, the ice droplets melted within 10 s. If the sample is tilted, the melted water droplet could easily slide off with little drag, indicating the film has good de-icing properties at low temperatures. In contrast, ice on the bare aluminum plate cannot be melted even under IR illumination for several minutes. From the icing/de-icing test in Fig. S5, it showed that the as-prepared composite film remained good superhydrophobic performance after 6 icing/de-icing cycles.

The excellent anti-icing and de-icing performance of the MWNT-0.7 composite films can be explained through the heat transfer model between droplets and the surfaces, as shown in Figs. 5b-d. Water droplets were suspended over the hierarchical structures for the anti-icing process, presenting Cassie's state. As shown in Fig. 5b, the total heat loss (ΔQ_l) was mainly attributed to three terms in an outdoor environment, defined in eq. (1a) [53,54]:

$$\Delta Q_l = Q_{cl} + Q_{rl} + Q^*_{rl} \tag{1a}$$

where Q_{cl}, Q_{rl} and Q^*_{rl} are the conduction heat loss, the convection heat loss, and the heat loss by thermal radiation at the triple-phase interface. Therefore, a superhydrophobic surface can significantly reduce the heat loss of water droplets through multi-phase interfaces. This was impossible on the bare aluminum plates, where the heat loss rate was dramatically increased due to its complete wetting state [54]. It can be concluded that the SMEP composite film can enhance the removal possibilities of supercold water by slowing the heat exchange. For de-icing, the heat transfer process on SMEP composite film is different because of its excellent photothermal property, see Fig. 5c. In this situation, water droplets could gradually obtain heat power by conduction (Q_{cg}) and heat radiation from an air cushion (Q^*_{rg}). Meanwhile, it also suffered from heat loss by natural convection (Q_{rl}). As illustrated in Fig. 5d, the heat exchange can be expressed as eq. (2) [55]:

$$\Delta Q = Q_{cg} + Q^*_{rg} - Q_{rl} \tag{2}$$

As a result, the spherical ice particles can quickly melt if the heat gained by conduction (Q_{cg}) and radiation from the air cushion (Q^*_{rl}) is larger than the heat loss. It is expected that the higher the photothermal efficiency is, the shorter the melting time will be. Therefore, the key point in enhancing the de-icing performance of photothermal materials is to increase solar-heat conversion efficiency for future applications.

To prove the performance of the composite films in a natural environment, outdoor experiments with freezing rain and snow have been carried out in winter in Harbin, northern China. The composite films were attached to the surface of a model airplane wing, as shown in Fig. 5e and supporting video 5. The cold water was dropped on the wings of an airplane model at the outdoor temperatures of −14 °C by mimicking the freezing rain situation. Water droplets quickly slid off the wing covered by the composite film resulting in the ice-free wing surface, see Figure 5f$_{\mathrm{I}}$. But water droplets were iced on the bare wing within 75 s. Figure 5f$_{\mathrm{II}}$ shows the thermography of the airplane model. The temperature of the aircraft wing covered with SMEP composite films could reach over 5 °C, but the bare aircraft wing was lower than −5 °C on average. The relatively high temperature of the composite film limited the possibility of ice formation.

To investigate the de-icing performance in snow, the experiments were carried out on a snowy day with an outdoor temperature of −10 °C. As shown in Fig. 5g and supporting video 6, both wings of the airplane were accumulated by a layer of snow. After the IR light was applied to the composite film, the snow on illuminated sections was gradually melted into water. Due to the low adhesion property of the film, the melted water actively self-coalesced into a water ball, as shown in the insets of Figure g$_{\mathrm{II}}$. The water droplets can be easily removed by wind or vibration due to the small contact area. Eventually, the illuminated areas were completely snow free, as shown in Figure g$_{\mathrm{III}}$.

Furthermore, an experiment was carried out to investigate the anti-icing and de-icing properties in extreme conditions with freezing rain and snow, see supporting video 7. As shown in Figure h$_{\mathrm{I}}$, the freezing rain effectively removed the snow on most segments of the film, although the ice was also inevitably formed. In contrast, on the bare airplane wing, the freezing rain accumulated on surfaces with snow simultaneously. This proved that the films could be a good candidate for freezing rain and snow prevention. When IR light was applied to the ice regions, the light directly acted on the interface through the ice layer, leading to the ice at the interface melting into the water until the residual ice slid off. Here, the melted water acted as the lubricant, as shown in Figures h$_{\mathrm{II}}$ and h$_{\mathrm{III}}$. Consequently, it proves that the composite film possesses good anti-icing and de-icing performance even in extreme conditions.

3.5. *Robustness and durability*

For potential outdoor applications, the films inevitably suffer from chemical and mechanical degradation, which might affect the superhydrophobic property and weaken the icephobic performance. As discussed in Section 3.2, one advantage of the SMEP composite films is that they can be easily attached and fitted to the complex outline of a facility when heated. The films will inevitably be heated and reshaped repeatedly in real applications. To test the thermal durability of a film, the film was heated over the T_g first, as shown in Fig. 6a. Then the film was folded four times into a cube at the temperature, producing sharp corners, see supporting video 8. The films were not raptured at the corner, even folded and pressed. After repeating this process 5 times, the film could recover to its original shape without damage. In addition, the film was boiled in hot water to test the thermal and chemical stability, as shown in Figure 6b$_{\mathrm{I}}$. After keeping in boiling water for 5 min, superhydrophobicity of the film could still be maintained, θ_{CA} of $\approx 150^\circ \pm 3^\circ$ and θ_{SA} of $\approx 8^\circ \pm 1^\circ$. When boiled for 15 min, the values of θ_{CA} and θ_{SA} were decreased slightly. The SEM image in Figure 6b$_{\mathrm{II}}$ demonstrates that the micro-nano structures of the film were not destroyed by boiling water. The EDS spectrum in Fig. S4a indicates that the characteristic elements of C, O, Si, and F remained even after boiling in water for 15 min. Especially, the F element was uniformly distributed on the composite film, as shown in Fig. S4b. Therefore, the film was well preserved without decomposition, making it present excellent durability under extreme conditions. We further examined the chemical stability of the film by exposure to solvent (ethanol) washing. It can be observed that after 5 times washing-drying treatments, water droplets were still suspended on the film, as shown in Fig. 6c. In addition, the films will suffer from various chemical corrosion conditions for real applications. Fig. 6d shows the relationship between pH value and the θ_{CA} and θ_{SA}. It is observed that the θ_{CA} and θ_{SA} fluctuated around 150° and 10° respectively, over a pH range from 1 to 14, indicating that pH values have little effect on the wettability of the film surface. Consequently, the film could be applied as a protective skin of a facility preventing corrosive liquids, such as acidic and alkaline solutions.

We have also inspected the physical robustness of the SMEP composite films through periodical sandpaper abrasion and water flushing tests. As shown in Fig. 6e, the mechanical stability was evaluated by pulling the film to slide across the sandpaper (360#) under normal pressure, which was controlled by the loading weight. As an extra load of 100 g (~2.6 kPa) was applied to the film, the values of θ_{CA} and θ_{SA} (see Fig. 6f) still maintained at $\approx 150^\circ$ and $\approx 11^\circ$ after 20 cm abrasion, respectively. With further increased abrasion distance to 40 cm, a slight decrease of the superhydrophobicity was observed, where θ_{CA} and θ_{SA} were $\approx 147^\circ$ and $\approx 15^\circ$, respectively. Meanwhile, the thickness of the film decreased greatly to 100 μm, as shown in the SEM images in Fig. 6g. Therefore, the superhydrophobic property was well preserved regardless of the surface damage. This should be attributed to the exposure of the newly generated hierarchical micro−/nano-structures after periodical sandpaper abrasion. In the high-speed water jet test (see Fig. 6h), the

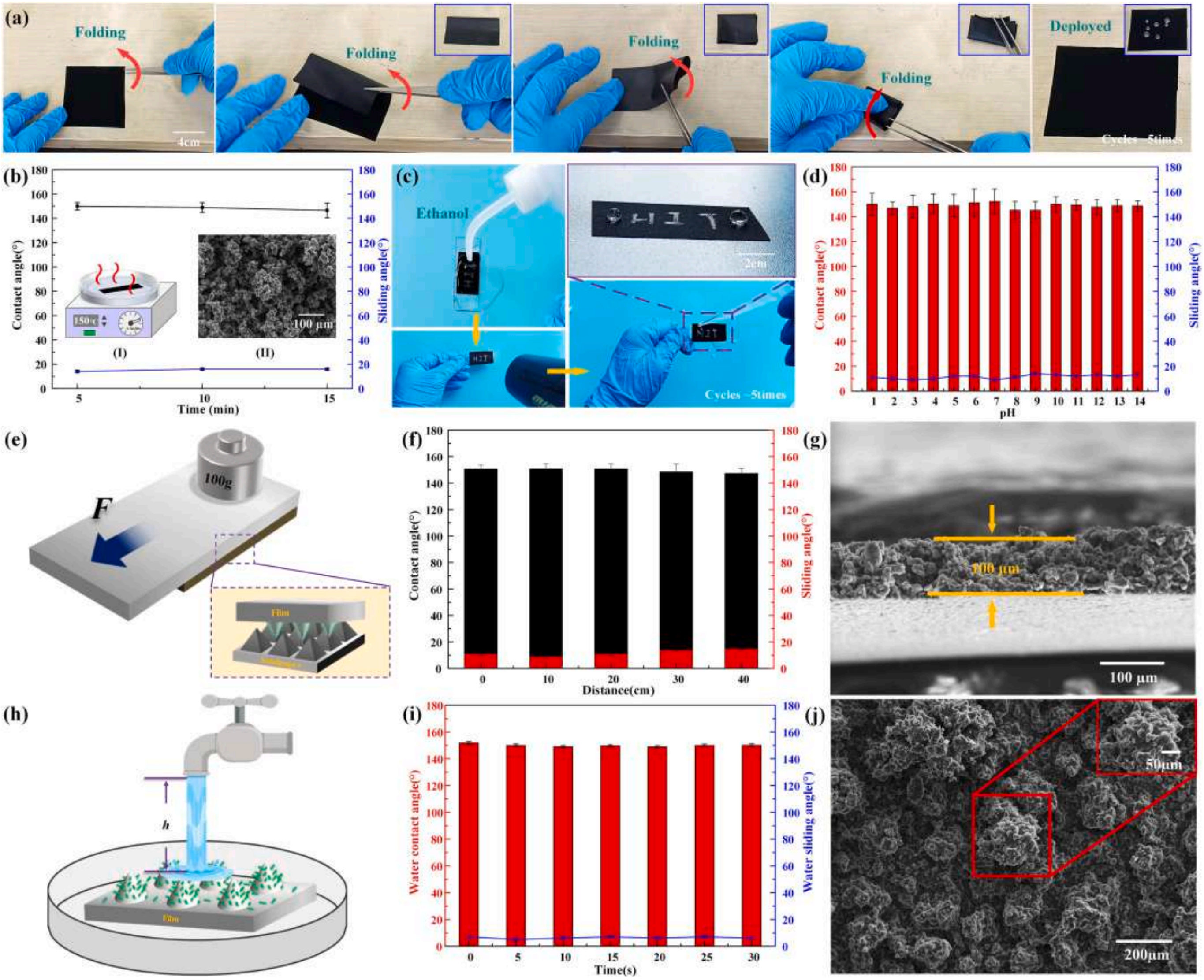

Fig. 6. (a) Thermal durability test; (b) Boiling water test; (c) Repeatedly washing-drying treatment of solvent; (d) Wettability of different pH values; (e) Schematic of the durability test via periodical sandpaper abrasion (grit #360); (f) Variation of θ_{CA} and θ_{SA} by a different distance of sandpaper abrasion; (g) Cross section of SEM images of SMEP composite films; (h) Schematic of high-speed water jet test with impacting pressure of 2.5 kPa; (i) Wettability at different flushing time; (j) SEM images of the hierarchical structures on SMEP composite films after flushed for 30 min.

film was fixed onto a glass plate flushed by a water stream under the tap. The impacting pressure of the water stream was 2.5 kPa, measured by placing a mechanical sensor at the same height as the tested film. The wetting performance of the film was investigated after each 5 min. As shown in Fig. 6i, there is no obvious degradation of superhydrophobic properties on the film, and the θ_{CA} and θ_{SA} maintained at 150° and 6° respectively, after flushing for 30 min. From the SEM images in Fig. 6j, it revealed that the hierarchical structures were maintained without damage, even at high flushing pressure. Consequently, the superior robustness of overall tests demonstrates that the SMEP composite films in this work can be a promising candidate for protective skin in real applications where waterproofing and flexibility are both demanded.

4. Conclusion

In summary, penguins-inspired superhydrophobic shape memory composite films with lightweight and shape-morphing properties have been successfully fabricated via spraying and peeling methods. The composite films present good superhydrophobic properties (WCA ~ 152.4 ± 5°, and WSA ~ 6 ± 1°) and shape memory performance (recovery ratio > 99%). It can memorize various shapes and recover to the original status under heat, IR light, and hot water with a T_g of 66 °C. Although the film has a thickness of 180 μm, it can withstand a total weight of 1.5 kg and remain undamaged after being repeatedly rolled by a vehicle (weight of ≈1559 kg) on a rough road. Meanwhile, the hierarchical micro-nano structures of films exhibited good light absorption performance in a wide wavelength range. Besides, the films presented good anti-icing and de-icing performance because of superhydrophobicity and photothermal properties. The freezing time of water droplets on the films was dramatically prolonged 10 times compared to that on a bare aluminum plate (31 s). The solid ice droplets are melted within 10s under infrared light illumination. It can be concluded that increasing solar conversion efficiency helps to enhance the de-icing performance of photothermal materials based on the heat transfer model. The outdoor snow prevention tests also prove that the films possessed good photothermal performance in de-icing applications. Finally, the films maintain good robustness and durability after harsh tests, including repeated thermal cycles, boiling water, abrasion, and water flush. Therefore, the lightweight, shape morphing, and photothermal properties of the superhydrophobic shape memory composite film are promising materials for industrial anti-icing and de-icing applications.

Supplementary data to this article can be found online at https://doi.org/10.1016/j.susmat.2023.e00692.

CRediT authorship contribution statement

Xinlin Li: Conceptualization, Methodology, Investigation, Visualization, Writing – original draft. **Yanju Liu:** Conceptualization, Validation, Writing – review & editing. **Jinsong Leng:** Resources, Supervision, Writing – review & editing.

Declaration of Competing Interest

The authors declare that they have no known competing financial interests or personal relationships that could have appeared to influence the work reported in this paper.

Data availability

Data will be made available on request.

Acknowledgements

This work was supported by the following funds: National Natural Science Foundation of China (No. 12102105), China Postdoctoral Science Foundation (No. 2021M690834), and Postdoctoral Science Foundation of Heilongjiang Province (No. LBH-Z21156).

References

[1] H. Chen, Y. Wu, H. Xia, B. Jing, Q. Zhang, Review of ice-pavement adhesion study and development of hydrophobic surface in pavement deicing, J. Traffic Transport. Eng. (Engl. Ed.) 5 (2018) 224–238.
[2] A. Zarnani, P. Musilek, X. Shi, X. Ke, H. He, R. Greiner, Learning to predict ice accretion on electric power lines, Eng. Appl. Artif. Intell. 25 (2012) 609–617.
[3] B.P. Jelle, The challenge of removing snow downfall on photovoltaic solar cell roofs in order to maximize solar energy efficiency—research opportunities for the future, Energ. Build. 67 (2013) 334–351.
[4] Z.A. Janjua, B. Turnbull, S. Hibberd, K. Choi, Mixed ice accretion on aircraft wings, Phys. Fluids 30 (2018) 27101.
[5] J. Liu, J. Xu, H. Huang, H. Chen, Microwave deicing efficiency and dielectric property of road concrete modified using different wave absorbing material, Cold Reg. Sci. Technol. 174 (2020), 103064.
[6] W. Yu, X. Yi, M. Guo, L. Chen, State of the art and practice of pavement anti-icing and de-icing techniques, Sci. Cold. Arid. Reg. 6 (2014) 14–21.
[7] A. Muthumani, L. Fay, M. Akin, S. Wang, J. Gong, X. Shi, Correlating lab and field tests for evaluation of deicing and anti-icing chemicals: a review of potential approaches, Cold Reg. Sci. Technol. 97 (2014) 21–32.
[8] Z. Azimi Dijvejin, M.C. Jain, R. Kozak, M.H. Zarifi, K. Golovin, Smart low interfacial toughness coatings for on-demand de-icing without melting, Nat. Commun. 13 (2022) 1–12.
[9] H. Ba, L. Truong-Phuoc, T. Romero, C. Sutter, J. Nhut, G. Schlatter, G. Giambastiani, C. Pham-Huu, Lightweight, few-layer graphene composites with improved electro-thermal properties as efficient heating devices for de-icing applications, Carbon 182 (2021) 655–668.
[10] Z. He, C. Wu, M. Hua, S. Wu, D. Wu, X. Zhu, J. Wang, X. He, Bioinspired multifunctional anti-icing hydrogel, Matter-Us 2 (2020) 723–734.
[11] H. Gao, Y. Jian, Y. Yan, The effects of bio-inspired micro/nano scale structures on anti-icing properties, Soft Matter 17 (2021) 447–466.
[12] D. Wang, Q. Sun, M.J. Hokkanen, C. Zhang, F. Lin, Q. Liu, S. Zhu, T. Zhou, Q. Chang, B. He, Design of robust superhydrophobic surfaces, Nature 582 (2020) 55–59.
[13] J. Kim, J. Jeon, D.R. Kim, K. Lee, Quantitative analysis of anti-freezing characteristics of superhydrophobic surfaces according to initial ice nuclei formation time and freezing propagation velocity, Int. J. Heat Mass Transf. 126 (2018) 109–117.
[14] V. Vercillo, S. Tonnicchia, J.M. Romano, A. García Girón, A.I. Aguilar Morales, S. Alamri, S.S. Dimov, T. Kunze, A.F. Lasagni, E. Bonaccurso, Design rules for laser-treated icephobic metallic surfaces for aeronautic applications, Adv. Funct. Mater. 30 (2020) 1910268.
[15] G. Zhang, Z. Wu, Q. Xia, Y. Qu, H. Pan, W. Hu, L. Zhao, K. Cao, E. Chen, Z. Yuan, Ultrafast flame-induced pyrolysis of poly (dimethylsiloxane) foam materials toward exceptional superhydrophobic surfaces and reliable mechanical robustness, ACS Appl. Mater. Interfaces 13 (2021) 23161–23172.
[16] D. Li, L. Ma, B. Zhang, S. Chen, Large-scale fabrication of a durable and self-healing super-hydrophobic coating with high thermal stability and long-term corrosion resistance, Nanoscale 13 (2021) 7810–7821.
[17] Y. Liu, X. Tan, X. Li, T. Xiao, L. Jiang, S. Nie, J. Song, X. Chen, Eco-friendly fabrication of transparent superhydrophobic coating with excellent mechanical robustness, chemical stability, and long-term outdoor durability, Langmuir 38 (2022) 12881–12893.
[18] L. Jiang, P. Hou, S. He, M. Han, P. Xiang, T. Xiao, X. Tan, The robust superhydrophobic SiO2/diatomite/PDMS/KH-570/Me-MQ composite coating for self-cleaning application of building surface, Colloids Surf. A Physicochem. Eng. Asp. 634 (2022), 127936.
[19] L.F. Mobarakeh, R. Jafari, M. Farzaneh, Robust icephobic, and anticorrosive plasma polymer coating, Cold Reg. Sci. Technol. 151 (2018) 89–93.
[20] R. Pan, H. Zhang, M. Zhong, Triple-scale superhydrophobic surface with excellent anti-icing and icephobic performance via ultrafast laser hybrid fabrication, ACS Appl. Mater. Interfaces 13 (2020) 1743–1753.
[21] L. Jiang, M. Han, J. Sun, M. Gong, Y. Lin, T. Xiao, P. Xiang, W. Chen, X. Tan, Strong mechanical and durable superhydrophobic photothermal MWCNTs/SiO2/PDMS/PVDF composite coating for anti-icing and de-icing, Prog. Org. Coat. 174 (2023), 107282.
[22] M. Yu, X. Li, X. Tan, X. Chen, Fluorine-free preparation of superhydrophobic coating with anti-icing property, mechanical durability and self-cleaning effect, Soft Matter 19 (2023) 766–775.
[23] T. Zhu, Y. Cheng, J. Huang, J. Xiong, M. Ge, J. Mao, Z. Liu, X. Dong, Z. Chen, Y. Lai, A transparent superhydrophobic coating with mechanochemical robustness for anti-icing, photocatalysis and self-cleaning, Chem. Eng. J. 399 (2020), 125746.
[24] Z. Li, Z. Zhen, M. Chai, X. Zhao, Y. Zhong, H. Zhu, Transparent electrothermal film defoggers and antiicing coatings based on wrinkled graphene, Small 16 (2020) 1905945.
[25] Y. Wang, Y. Sun, Y. Xue, X. Sui, F. Wang, W. Liang, Q. Dong, Multifunctional electro-thermal superhydrophobic shape memory film with in situ reversible wettability and anti-icing/deicing properties, Colloids Surf. A Physicochem. Eng. Asp. 654 (2022), 129960.
[26] T. Cheng, R. He, Q. Zhang, X. Zhan, F. Chen, Magnetic particle-based super-hydrophobic coatings with excellent anti-icing and thermoresponsive deicing performance, J. Mater. Chem. A 3 (2015) 21637–21646.
[27] W. Zheng, L. Teng, Y. Lai, T. Zhu, S. Li, X. Wu, W. Cai, Z. Chen, J. Huang, Magnetic responsive and flexible composite superhydrophobic photothermal film for passive anti-icing/active deicing, Chem. Eng. J. 427 (2022), 130922.
[28] W. Niu, G.Y. Chen, H. Xu, X. Liu, J. Sun, Highly transparent and self-healable solar thermal anti-/deicing surfaces: when ultrathin MXene multilayers marry a solid slippery self-cleaning coating, Adv. Mater. 34 (2022) 2108232.
[29] S. Wu, Z. Liang, Y. Li, S. Chay, Z. He, S. Tan, J. Wang, X. Zhu, X. He, Transparent, Photothermal, and Icephobic surfaces via layer-by-layer assembly, Adv. Sci. 2105986 (2022).
[30] S. Dash, J. de Ruiter, K.K. Varanasi, Photothermal trap utilizing solar illumination for ice mitigation, Sci. Adv. 4 (2018), t127.
[31] E. Alizadeh-Birjandi, F. Tavakoli-Dastjerdi, J.S. Leger, K.F. Faull, S.H. Davis, J. P. Rothstein, H. Pirouz Kavehpour, Delay of ice formation on penguin feathers, Eur. Phys. J.-Spec. Top. 229 (2020) 1881–1896.
[32] J. Su, X. Xie, L. Wang, X. Gao, J.J. Klemes, Novel bionic and clean de-icing bituminous composite material by autocrine microcapsule production with a temperature responsive character, J. Clean. Prod. 311 (2021).
[33] Y. Xia, Y. He, F. Zhang, Y. Liu, J. Leng, A review of shape memory polymers and composites: mechanisms, materials, and applications, Adv. Mater. 33 (2021) 2000713.
[34] A. Li, J. Fan, G. Li, Recyclable thermoset shape memory polymers with high stress and energy output via facile UV-curing, J. Mater. Chem. A 6 (2018) 11479–11487.
[35] Y.C. Sun, M. Chu, M. Huang, O. Hegazi, H.E. Naguib, Hybrid electroactive shape memory polymer composites with room temperature deformability, Macromol. Mater. Eng. 304 (2019) 1900196.
[36] F. Zhang, L. Wang, Z. Zheng, Y. Liu, J. Leng, Magnetic Programming of 4D Printed Shape Memory Composite Structures, Elsevier, 2019.
[37] Y. Chen, X. Zhao, C. Luo, Y. Shao, M. Yang, B. Yin, A facile fabrication of shape memory polymer nanocomposites with fast light-response and self-healing performance, Compos. A: Appl. Sci. Manuf. 135 (2020), 105931.
[38] Y. Guo, Z. Lv, Y. Huo, L. Sun, S. Chen, Z. Liu, C. He, X. Bi, X. Fan, Z. You, A biodegradable functional water-responsive shape memory polymer for biomedical applications, J. Mater. Chem. B 7 (2019) 123–132.
[39] Y. Sun, Z. Guo, Recent advances of bioinspired functional materials with specific wettability: from nature and beyond nature, Nanoscale Horiz 4 (2019) 52–76.
[40] Z.J. Cheng, D.J. Zhang, X. Luo, H. Lai, Y.Y. Liu, L. Jiang, Superwetting shape memory microstructure: smart wetting control and practical application, Adv. Mater. 33 (2021).
[41] Y. Jiang, U. Mansfeld, L. Fang, K. Kratz, A. Lendlein, Temperature-induced evolution of microstructures on poly [ethylene-co-(vinyl acetate)] substrates switches their underwater wettability, Mater. Design 163 (2019), 107530.
[42] Y. Wang, Y. Sun, Y. Xue, X. Sui, F. Wang, W. Liang, Q. Dong, Multifunctional electro-thermal superhydrophobic shape memory film with in situ reversible wettability and anti-icing/deicing properties, Colloids Surf. A Physicochem. Eng. Asp. 654 (2022), 129960.
[43] L. Chen, Y.S. Zhang, Z.Q. Liu, Q.H. Song, C.Z. Liu, Effect of graphene oxide doping on anti−/deicing performance of shape memory epoxy resin, Mater. Today Commun. 30 (2022).
[44] Y. Shen, X. Wu, J. Tao, C. Zhu, Y. Lai, Z. Chen, Icephobic materials: fundamentals, performance evaluation, and applications, Prog. Mater. Sci. 103 (2019) 509–557.

[45] T. Zhu, Y. Ni, K. Zhao, J. Huang, Y. Cheng, M. Ge, C. Park, Y. Lai, A breathable knitted fabric-based smart system with enhanced superhydrophobicity for drowning alarming, ACS Nano 16 (2022) 18018–18026.

[46] S. Yang, Y. He, Y. Liu, J. Leng, Shape-memory poly (arylene ether ketone) s with tunable transition temperatures and their composite actuators capable of electric-triggered deformation, J. Mater. Chem. C 8 (2020) 303–309.

[47] J. Zhang, W. Zhang, J. Lu, C. Zhu, W. Lin, J. Feng, Aqueous epoxy-based superhydrophobic coatings: fabrication and stability in water, Prog. Org. Coat. 121 (2018) 201–208.

[48] C. Guo, H. Ding, M. Xie, H. Zhang, X. Hong, L. Sun, F. Ding, Multifunctional superamphiphobic fluorinated silica with a core-shell structure for anti-fouling and anti-corrosion applications, Colloids Surf. A Physicochem. Eng. Asp. 615 (2021), 126155.

[49] X. Yu, S. Zhou, X. Zheng, T. Guo, Y. Xiao, B. Song, A biodegradable shape-memory nanocomposite with excellent magnetism sensitivity, Nanotechnology 20 (2009), 235702.

[50] W. Li, Y. Liu, J. Leng, Selectively actuated multi-shape memory effect of a polymer multicomposite, J. Mater. Chem. A 3 (2015) 24532–24539.

[51] L. Luo, F. Zhang, J. Leng, Multi-performance shape memory epoxy resins and their composites with narrow transition temperature range, Compos. Sci. Technol. 213 (2021), 108899.

[52] Y. Hu, K. Cao, H. Rong, J. Xu, H. Han, H. Wang, L. Pattelli, N. Li, H. Xu, J. Zhao, Sprayable Ultrablack coating based on hollow carbon nanospheres, Acs Appl. Nano Mater. 4 (2021) 7995–8002.

[53] P. Guo, Y.M. Zheng, M.X. Wen, C. Song, Y.C. Lin, L. Jiang, Icephobic/anti-icing properties of Micro/nanostructured surfaces, Adv. Mater. 24 (2012) 2642–2648.

[54] X. Li, G. Wang, A.S. Moita, C. Zhang, S. Wang, Y. Liu, Fabrication of bio-inspired non-fluorinated superhydrophobic surfaces with anti-icing property and its wettability transformation analysis, Appl. Surf. Sci. 505 (2020).

[55] Z. Xie, H. Wang, Y. Geng, M. Li, Q. Deng, Y. Tian, R. Chen, X. Zhu, Q. Liao, Carbon-based Photothermal Superhydrophobic materials with hierarchical structure enhances the anti-icing and Photothermal deicing properties, ACS Appl. Mater. Interfaces 13 (2021) 48308–48321.